



High-speed label-free confocal microscopy of *Caenorhabditis elegans* with near infrared spectrally encoded confocal microscopy

SADAF RASHTCHIAN, KHALED YOUSSEF, POUYA REZAI, AND NIMA TABATABAEI* 

Mechanical Engineering Department, Lassonde School of Engineering, York University, Toronto, Canada

*nima.tabatabaei@lassonde.yorku.ca

Abstract: *Caenorhabditis elegans* (*C. elegans*) is an optically transparent nematode that shares many gene orthologs and homologs with humans. *C. elegans* are widely used in large populations for genetic studies relevant to human biology and disease. Success of such studies frequently relies on the ability to image *C. elegans* structure at high-resolution and high-speed. In this manuscript, we report on the feasibility and suitability of a high-speed variant of reflectance confocal microscopy, known as spectrally encoded confocal microscopy (SECM), for label-free imaging of *C. elegans*. The developed system utilizes near-infrared illumination in conjunction with refractive and diffractive optics to instantaneously image a confocal image line at a speed of up to 147 kHz with lateral and axial resolutions of 2 μm and 10 μm , respectively. Our imaging results from wild-type *C. elegans* and four mutant strains (MT2124, MT1082, CB61, and CB648) demonstrate the ability of SECM in revealing the overall geometry, key internal organs, and mutation-induced structural variations, opening the door for downstream integration of SECM in microfluidic platforms for high throughput structural imaging of *C. elegans*.

© 2021 Optical Society of America under the terms of the [OSA Open Access Publishing Agreement](#)

1. Introduction

Caenorhabditis elegans (*C. elegans*) is a popular model organism for studying a broad spectrum of human diseases [1]. These free-living nematodes have a short lifecycle (~three weeks) and are optically transparent [2]. Most importantly, *C. elegans* have a fully sequenced genome and share many gene orthologs and homologs with humans (many of which are related to human diseases [3]). Different human disorders such as neurodegenerative diseases [4], diabetes [5], and cancer have been modeled using *C. elegans* to further understand disease pathology and provide a model for drug discovery [2]. *C. elegans* neuronal, cellular, and behavioral phenotypes can offer reliable readouts of genetic mutation and drug screening. For instance, genetic mutations in lung cancer associated genes were found to cause a deficiency in *C. elegans* vulva development, or to induce a multi-vulva (Muv) phenotype [2]. The phenotypic screening of behaviors like pharyngeal pumping rate as a measure for food intake has also been utilized for drug screening due to the ease of monitoring the synchronous motion of the grinder movements [3]. For example, Parkinson's disease worms with alpha-synuclein mutation showed a significant decrease in their pharyngeal pumping rate, which was alleviated using anti-Parkinsonian compounds [2,3,6,7]. The success of the abovementioned biological investigations frequently relies on the ability to screen the structures of large populations of worms in order to reach statistically meaningful conclusions. Given the small size and optical transparency of *C. elegans*, often, imaging the worms at high resolution is necessary for interrogation and screening of cells and organs of interest (e.g., neurons, vulva, isthmus, corpus, and intestine).

Fluorescent microscopy techniques are normally the preferred interrogation method for studying *C. elegans* mutagenesis. To date, confocal fluorescent microscopy (CM), light sheet

fluorescent microscopy (LSFM), selective plane illumination microscopy (SPIM), and two-photon microscopy have been exploited to probe *C. elegans* cellular and neuronal activities. Fluorescent CM is frequently used for imaging live *C. elegans* [8]. The transparency of *C. elegans* allows proteins and neurons expressions to be imaged [1]; optical sectioning and 3D imaging are other key advantages of fluorescent CM. Photodamage and slow imaging speed are main limitations of CM which have been mostly overcome by LSFM and SPIM, respectively [9,10]. Two-photon fluorescent microscopy has also been implemented to obtain information on different cell types of *C. elegans* [11]. The common denominator of fluorescent microscopy techniques, however, is the reliance on fluorescent labeling that increases the sample preparation time and complexity and also can interfere with cellular processes [12]. Moreover, fluorescent-based techniques are not suitable for physiological and behavioral phenotype screening due to absence of fluorescence expression. For such applications, label-free structural microscopy technologies such as bright-field microscopy and differential interference contrast (DIC) microscopy are often used. However, bright-field microscopy offers limited contrast and lacks optical sectioning ability, making it difficult to reliably screen the internal organs. DIC, on the other hand, is an interferometric imaging method which offers high contrast pseudo-3D relief shading images of specimens [8]; but, DIC image brightness is less than bright field microscopy which makes sample illumination challenging at high magnifications. Lack of optical sectioning and 3D imaging in DIC is another limitation of the technique, leading to superposed and blurry DIC micrographs of *C. elegans* internal organs [12]. This brief review of *C. elegans* microscopy landscape highlights the need for high-speed imaging platforms that offer high-resolution confocal images to enable high-throughput physiological and behavioral phenotype screening of *C. elegans* based on their intrinsic contrast and geometry.

Spectrally encoded confocal microscopy (SECM) is a high-speed and fiber-optic-based variant of reflectance confocal microscopy with great potential to address this need [13]. In SECM, a diffraction grating-objective lens pair is used to focus/encode different wavelengths of a broadband laser light on a transverse confocal line inside the sample while reflections from the confocal line are continuously recorded with a spectrometer [13]. Enhancement of imaging speed in SECM is due to the ability to instantaneously image a confocal line. To form two dimensional images, the confocal line can be laterally translated via a scanning mirror, or alternatively, the sample can be translated through the stationary confocal line [14]. The native field of view (FOV) of SECM, however, is limited to that of the objective lens. To overcome this limitation, several sample translation and image stitching strategies have been reported. For example, SECM imaging of extended biological samples has been demonstrated via two dimensional translation of samples *ex vivo* [15], or via translating endoscopic probes [16], and swallowable capsules [17], with internal spinning SECM optics *in vivo*. The possibility of performing SECM imaging with scan-free confocal optics has also been demonstrated in both bench-top [18,19], and low-cost handheld [20,21], systems. While these scanning strategies can be utilized for SECM imaging of *C. elegans*, the small native FOV of SECM is often sufficient since the diameter and length of the gravid adult *C. elegans* are only ~50–80 μm and ~1 mm, respectively [1]. Presence of speckle in images is another key limitation of SECM when imaging biological tissues. While image speckle is often minimized through adherence to a multimode detection scheme [22], or the use of spatially incoherent light sources [21], image speckle is not expected to be a limitation for imaging *C. elegans* because these nematodes, unlike human tissue, are mostly transparent.

To date, SECM has only occasionally been used to image small organisms. Boudoux *et al.* demonstrated *in vivo* SECM imaging of *Xenopus laevis* myocardium and Zebrafish embryo [14]. To the best of our knowledge, SECM imaging of *C. elegans* has not been explored yet. In this feasibility study, we report on the development of a near infrared (NIR) SECM system for label-free and high-speed confocal imaging of *C. elegans*. Our results show the possibility of not only visualizing the size and geometry of the nematode but also resolving the key internal

organs that are the target of many human disease models. Results of four case studies on different mutations of *C. elegans* (MT2124, MT1082, CB61, and CB648) demonstrate feasibility of resolving mutation-induced structural abnormalities with NIR SECM. Given the high-speed trait of SECM, this work can open the door for downstream integration of SECM in microfluidic platforms for high throughput physiological and behavioral phenotype screening of *C. elegans* populations.

2. Methods

2.1. SECM system

The schematic of the developed SECM system is depicted in Fig. 1(a). In this system, the broadband laser light of the laser source (1311 nm; FWHM = 103 nm, Exalos Inc, Switzerland) is coupled into a single mode optical fiber (SMF-28). After passing through a variable fiber-optic attenuator, light enters the first port of an optical circulator and subsequently enters the imaging arm via the circulator's second port. In the imaging arm, light is collimated (via L1) to a 3 mm spot size, reflected off a 1-D galvanometric (galvo) mirror scanner (Thorlabs Inc, USA), and directed to a transmission diffraction grating (HD 1145 l/mm: Wasatch Photonics, USA) at the Littrow angle. Through a custom-made telescope (L2 and L3) the diffracted beam fills the back aperture of a long working distance NIR objective lens (Mitutoyo, Plan Apo NIR 20X/0.4 NA, and 50X/0.42 NA) which, in return, focuses different wavelengths of the laser source on a line (aka. spectrally encoded line; See Fig. 1(a) inset). Reflected light from the spectrally encoded line transmits back through the imaging arm and couples to the optical fiber through lens L1. The core of the fiber effectively acts as the illumination and detection pinholes of the confocal microscopy system, rejecting the out of focus light. Eventually, the reflected light from the sample is delivered to a spectrometer with a maximum line rate of 147 KHz (Cobra 1300; Wasatch photonics) via the third port of the optical circulator. Given these system specifications, the theoretical spectral resolution of the grating in the imaging head was calculated as 0.2285 nm. With such grating spectral resolution, the system can resolve 450 points in the wavelength dispersed axis (1260 – 1363 nm) [23,24]. In order to achieve Nyquist sampling, we need to sample at least 1364 pixels per spectrally-encoded line [25], which is achievable with the 0.075 nm spectral resolution of our spectrometer. However, the number of resolvable points in our system is limited by the objective spot size (1.83 μm) and calculated as 333 points across the theoretical 611 μm spectrally-encoded line [23].

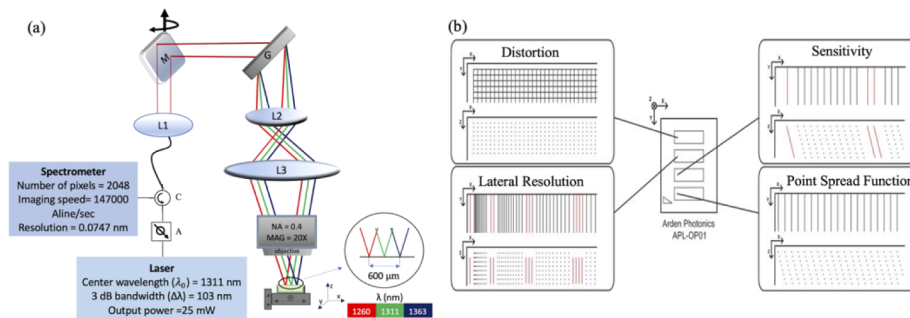


Fig. 1. (a) schematic of SECM system. A: attenuator C: circulator, L1: collimator, M: galvanometer mirror, G: diffraction grating, L2, L3: telescopic beam expander, (b) Schematic of the APL-OP01 patterns; reprinted with permission.

To form 2D confocal images, a custom-made program was developed in the LabVIEW environment to synchronously move the galvanometric mirror to produce $\sim 200 \mu\text{m} \times 600 \mu\text{m}$

images with 20X objective at an imaging speed up to 300 Hz. To ensure accurate and repeatable positioning of the sample in the confocal plane, the sample platform was equipped with three compact motorized translation stages (Thorlabs Inc., USA) with minimum movement step size and bidirectional repeatability of 0.05 μm and 1.6 μm , respectively. With respect to the objective lens used in our system, it should be noted that dry objectives are generally more prone to spherical aberrations and image degradation with the increase in imaging depth than water immersion objectives; however, the significantly longer working distance of the dry objective used in our system is expected to facilitate better downstream integration of SECM in microfluidic platforms that often contain multiple bulky components on their interrogated surface (e.g., inlets, outlets, tubes and micro pumps).

2.2. Performance tests

To evaluate the optical performance of the SECM system, several benchmark tests were carried out. Line distortion, lateral resolution, and point spread function were assessed by imaging the corresponding segments of the Arden validation phantom (APL-OP01, Arden Photonics; Fig. 1(b)) [26]. These segments are comprised of 8 layers of reflective line patterns; the first layer is located 100 μm below the top surface, and axial spacing between the layers is 75 μm . The distortion pattern has 100 \times 100 μm^2 square reflective grids. In the point spread function, there are series of lines in each layer separated by 150 μm . Each layer is laterally offset by a 25 μm distance from the next layer. The lateral resolution pattern is comprised of groups of 11 reflective lines with varying lateral spacing. Each line in this pattern is separated laterally from the next by a distance, starting at 1 μm and increasing by increments of 1 μm . Once the group and line numbers of line pairs that just blur together are identified, a reference equation is used to estimate the lateral resolution. To measure system's axial resolution, a mirror was scanned through the focus with a 0.5- μm step size. The full width at half maximum (FWHM) of the intensity profile was considered as the axial resolution of the SECM system.

2.3 *C. elegans* strains, maintenance, and synchronization

Wild-type (WT) (N2) as well as MT2124, MT1082, CB61, and CB648 strains were obtained from the *Caenorhabditis* Genetics Center (University of Minnesota, Minneapolis, MN, USA) (Table 1) and grown on standard nematode growth media agar plates (NGM) prepared with *Escherichia coli* OP50 as a food source at room temperature ($\sim 22^\circ\text{C}$) [27]. A freshly prepared Luria Broth (LB) media (10 g bacto-tryptone, 5 g bacto-yeast, and 5 g NaCl in 1 L distilled water) was inoculated with a single OP50 colony and cultured overnight in a thermal shaker incubator at 37 $^\circ\text{C}$. The NGM plates were seeded with 100 μL of the bacterial culture and left to dry overnight at room temperature. *C. elegans* maintenance was performed under Biosafety protocol Number 02–19 issued by York University's Biosafety Committee to PR.

Table 1. *C. elegans* strains used in this study.

Strain	Genotype	Description
N2	WT Bristol	Wild type
MT2124	let-60(n1046)	Multivulva phenotype [29].
MT1082	egl-1(n487) V	Egg-laying defective, Retains late-stage eggs [30].
CB61	dpy-5(e61) I	Strong dumpy; early larvae non-Dpy [31].
CB648	vab-3(e648) X	Notched head [32].

All experiments were conducted with age-synchronized worms using the Alkaline hypochlorite treatment [28]. Briefly, well-fed gravid adult worms were washed off plates in a 15 mL Eppendorf tube using M9 buffer (3 g KH_2PO_4 , 6 g Na_2HPO_4 , 5 g NaCl, and 1 ml 1 M MgSO_4 in 1 L distilled water). Then, the worms were treated for 10 minutes according to Porta-de-la-Riva *et*

al. protocol [28], using a commercial bleach solution (3.875 mL double-distilled water, 125 μ L NaOH, and 1 mL commercial bleach). Following the treatment, the eggs were collected and incubated in 1 mL M9 buffer and allowed to hatch overnight. The hatched L1 larvae were plated on freshly prepared NGM and allowed to grow to the gravid adult stage, except for starved worms. To obtain starved worms, gravid adult worms were manually picked to a freshly prepared unseeded NGM plate until starvation. For imaging, worms were individually picked and fixed between two microscope coverslips with a droplet of M9 containing 25 mM of sodium azide [29]. Sodium azide has been extensively used as an anesthetic for *C. elegans* to slow or stop its movement for high-resolution imaging. The worms generally stopped moving within a minute or two.

3. Results and discussion

3.1. Performance tests

The SECM image of the first layer of phantom's distortion pattern is depicted in Fig. 2(a); this pattern is imaged with a 20X/0.4 NA objective lens. While no obvious distortion is observed in the spectrally encoded direction, a slight curvature of lines can be seen in the galvo scanning direction. This distortion can be related to non-optimal scanning of beam over the back aperture of objective [33]; however, the induced distortion is minimal (less than 2 μ m shift over a 100 μ m-line) and not expected to be significant when imaging *C. elegans*. The 3D render of all eight layers can be seen in Fig. 1(b). It demonstrates the system's ability to image layered grid patterns spanning 600 μ m in depth without any noticeable distortion. Using the distortion pattern's 100 \times 100 μ m² cell size as a reference, the optimal field of view (FOV) with the 20X objective in the spectrally encoded and galvo scanning directions were measured as 600 μ m and 200 μ m, respectively. The measured 600 μ m optimal length of the spectrally encoded line corresponds to the FWHM of the light source and was theoretically calculated as 611 μ m. The small difference between the estimated and measured values can be due to small misalignment of telescope lenses leading to slightly smaller angular deviation of wavelength extremities at the back aperture of the objective lens.

Panels c and d show the resolution patterns of the Arden phantom acquired with the 20X objective lens in the galvo scanning and spectrally encoded directions, respectively. To measure the resolution, the first group of the pattern, which contains the minimum line spacing, was fitted to the FOV of the system. The magnified images of panels c and d show that lines 1 and 2 cannot be reliably differentiated from each other but the separation of line 2 (white arrowhead) from line 3 (red arrowhead) can clearly be recognized in both spectrally encoded and galvo scanning directions. As such, based on Arden phantom reference equation, system's lateral resolution is estimated to be \sim 2 μ m. This estimation is consistent with our lateral resolution measurements with the line spread function method of 2.17 μ m and 2.08 μ m in the galvo scanning and spectrally encoded directions, respectively. However, the measured lateral resolution is inferior to the one estimated from Rayleigh criterion (e.g., 2.08 μ m vs 1.83 μ m), leading to number of resolvable points in the spectrally encoded direction smaller than the theoretical value (600 μ m/2.08 μ m = 288 points vs 333 points). We hypothesize that the difference between estimated and experimental values is due to the aberrations introduced by the objective lens.

Figure 2(e) shows the measured PSFs along depth of the phantom. The PSF pattern is often used to evaluate the degradation of lateral resolution along the depth due to aberrations [34]. Comparison of the FWHM of the normalized curves shows that moving the confocal image plane 600 μ m in glass medium yields minimal deterioration of PSF. The average FWHM of PSF was measured as 2.17 ± 0.3 μ m which is consistent with measurements made with the lateral resolution pattern. Figure 2(f) depicts the axial response of the SECM system using the 20X objective lens. The FWHM of the axial response curve was measured to be 10 μ m. The theoretical value for axial resolution was calculated at 8.2 μ m. The difference between estimated

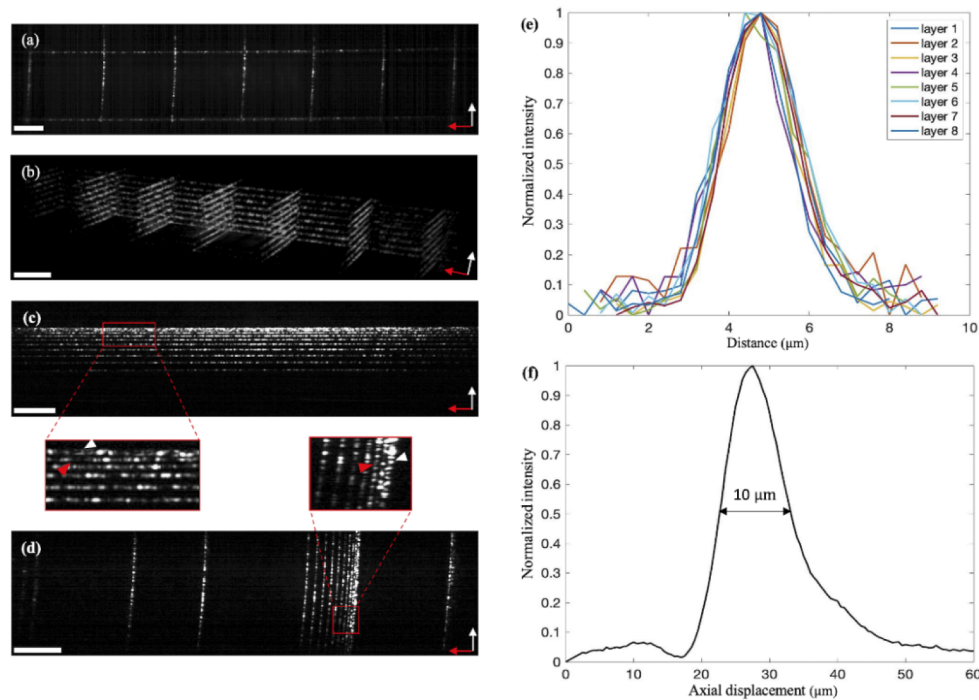


Fig. 2. (a) SECM image of the first layer of distortion pattern, (b) 3D render of patterns in distortion group in all layers. First group of the lateral resolution pattern of the phantom in (c) galvo scanning and (d) spectrally encoded directions. The white and red arrowheads in the magnified panels show the second and third lines of the group one in lateral resolution pattern. (e) Normalized PSFs of the eight layers of the APL-OP01. (f) System's axial response obtained by scanning a mirror through the focus, the FWHM is 10 μm . In panels (a)-(d) white and red arrows indicate galvo scanning and spectrally encoded directions. Scale bar = 50 μm .

and measured axial resolutions can be due to the spherical aberration of lens, leading to the broadening of the PSF compared to the diffraction limited one.

3.2 Adult WT *C. elegans* SECM imaging

Figure 3(a) shows a large area SECM image of a gravid adult worm. To accommodate the extended length of the adult worm, this 1.3 mm \times 200 μm image was produced by stitching 3 iso-depth SECM images with ImageJ software [35]. Aside from the overall geometry and size of the worm, key internal organs can be resolved. For example, in the pharyngeal region, procorpus, metacarpus, isthmus, and posterior bulb can be seen in the SECM image. High-speed and high-resolution visualization of these organs is critical for a spectrum of disease models. For example, the contractions in pharynx are important in studies related to feeding behavior of *C. elegans* [3]. The intestine of the worm is also visible along the body (from head to gut). Imaging the intestine is vital in disease studies related to fat storage disorders, diabetes, and metabolic syndrome [5,36]. In the middle part of the worm, the uterus is located where the eggs are stored and deposited through the vulva. Vulva and egg development are routinely studied in aging and reproduction assays.

Figure 3(b) shows the SECM image of a young adult *C. elegans*. The SECM image, clearly, resolves key organs in the head region such as mouth, procorpus, metacarpus, isthmus, and posterior bulb as well as other body organs such as gonad and a developing vulva. The length of this worm is measured as 860 μm with a diameter of \sim 50 μm which is smaller than the adult *C.*

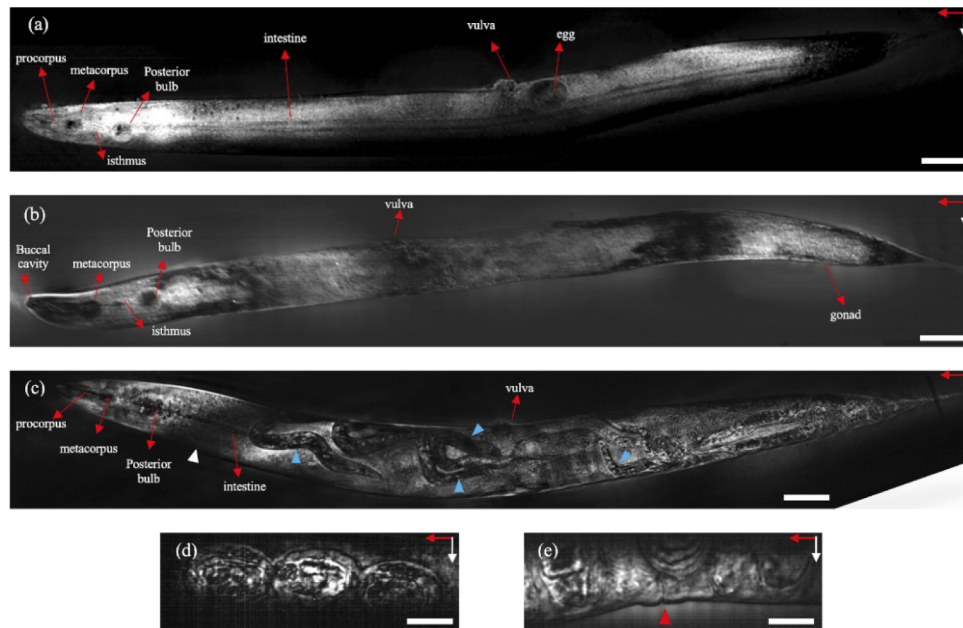


Fig. 3. SECM images showing different internal organs of (a) an adult *C. elegans*, (b) *C. elegans* in the young adult stage, (c) worm-bagged *C. elegans* with larvae inside it (blue arrowheads). High magnification images of (d) eggs and (e) vulva (red arrowhead) of an adult *C. elegans* obtained with 50X objective. White and red arrow showing galvo scanning and spectrally encoded direction respectively. Scale bar = 50 μm .

C. elegans of panel (a), as expected. Figure 3(c) depicts a starved worm with several L1 worms inside the body (blue arrowheads). Parent's pharyngeal region, intestine, and vulva are also visible in this image. The dark region (white arrowhead) is a stitching artifact and not from the sample. Figures 3(d) and 3(e) show high resolution SECM images of the eggs and vulva of an adult *C. elegans*, acquired with the 50X objective lens. The higher magnification allows for resolution of internal cellular constituents of the eggs, albeit at the cost of smaller FOV. SECM images of Fig. 3 demonstrate feasibility of resolving WT *C. elegans* key internal organs such as the pharyngeal region (mouth, isthmus, posterior bulb, and terminal bulb), vulva, egg, hatched larvae and lumen of the intestine at high resolution, and with high contrast, without the use of labels/stains. In addition, SECM imaging of *C. elegans* is not prone to speckle noise, unlike that of human soft tissue.

To confirm system's optical sectioning ability, a gravid adult worm was axially scanned in 15 μm steps. Figure 4(a) depicts four axial image slices of the *C. elegans* head demonstrating appearance and disappearance of features along the depth. The first image is taken from the top of the worm body. First image shows the structure of the head and the mouth while the pharyngeal region is not visible. As the pharynx is structurally located in the middle sections, it becomes more visible as we scan closer to the mid-body and it then starts to fade away as the confocal imaging plane advances deeper. In the last slice, we are about to reach the other side of the body, and the entire pharyngeal region is slowly fading away. SECM images of Fig. 4 demonstrate the slicing and depth-selective nature of system.

One of the appealing characteristics of SECM is its high imaging speed which enables time-lapse confocal imaging of organs and/or body sections. Representative frames from the movement of head of a WT *C. elegans* are depicted in Fig. 4(b). The SECM time-lapse images can potentially be segmented and quantitatively analyzed to calculate the speed and frequency of

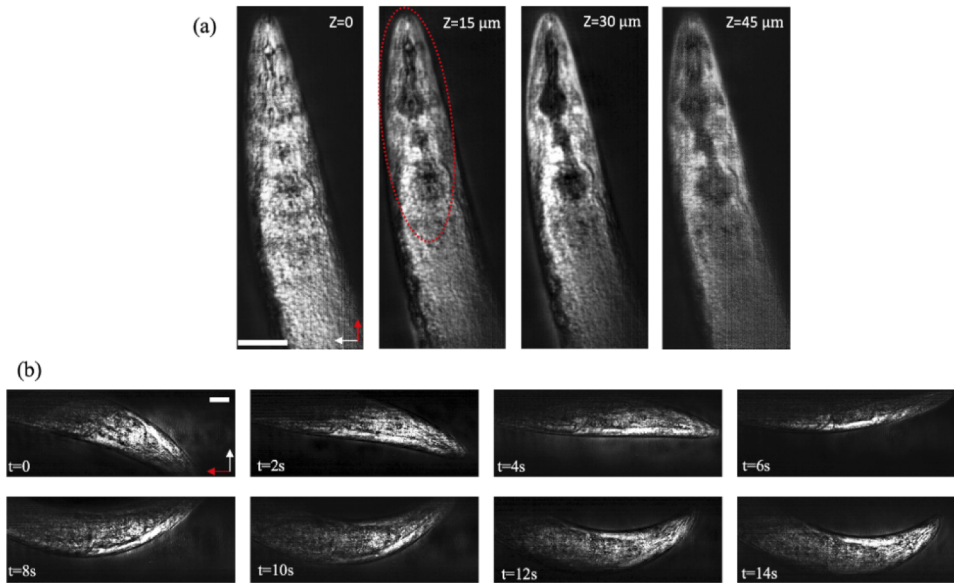


Fig. 4. (a) Representative z-stack images of *C. elegans* pharyngeal region, (b) Representative frames from movement of at 2-second intervals. White and red arrows showing galvo scanning and spectrally encoded direction respectively. Scale bar = 50 μm .

C. elegans movement that is key for several categories of behavioral studies [37]. For example, correlation of maximum pharyngeal pumping rate with age in adult WT *C. elegans* [3], can be studied with our SECM system at an *en face* image rate of ~ 10 KHz. Pharyngeal pumping is directly related to feeding regulation and often used as a phenotype for studying obesity and type 2 diabetes [36,37]. Visualization 1 shows real-time confocal imaging of movement of a dumpy *C. elegans* in a time span of 26 seconds which suggest feasibility of performing behavioral studies with SECM at high resolution and high speed. Given the sharp contrast of the mouth, procorpus, metacorpus, isthmus, and posterior bulb, we anticipate SECM imaging to be specifically valuable for screening feeding disorders in *C. elegans*.

3.3 Mutant *C. elegans* SECM Imaging

Studying the genetic and phenotypic aspects of *C. elegans* mutant strains is commonplace in biology. In an abundant number of cases, mutations result in alterations of the physiology of targeted organs in *C. elegans*, most of which can be resolved by SECM. For example, mutation in the MT2124 strain (Table 1) disrupts the intrinsic GTPase activity and causes protrusions on the worm body [7,38]. These protrusions are called psuedovulvae since they are not functional [39]. The MT2124 strain is also a popular mutant associated with juvenile myelomonocytic leukemia, cutaneous melanoma, and acute myeloid leukemia in humans [7]. Figure 5(a) presents an SECM image of a MT2124 worm with one psuedovulva (white arrowhead). Psuedovulva can clearly be recognized in the confocal image due to its different shape and appearance from that of a normal vulva (red arrowhead); accumulations of eggs in the body are also clearly resolved in this image. SECM's ability in confocal resolution of vulva can be beneficial to *C. elegans* chemical screening and toxicity assays where the effective dose of chemicals on the shape, size, and formation of the vulva are investigated [7,39].

The *egl-1* gene is usually defined by GF (gain of function) mutations which can lead to the death of the hermaphrodite specific neurons (HSN). Since in *C. elegans* HSN is essential for egg-laying [40], the MT1082 strains are defective in reproduction and normally retain the late-stage eggs inside the body. Figure 5(b) is a representative SECM image of a MT1082 worm.

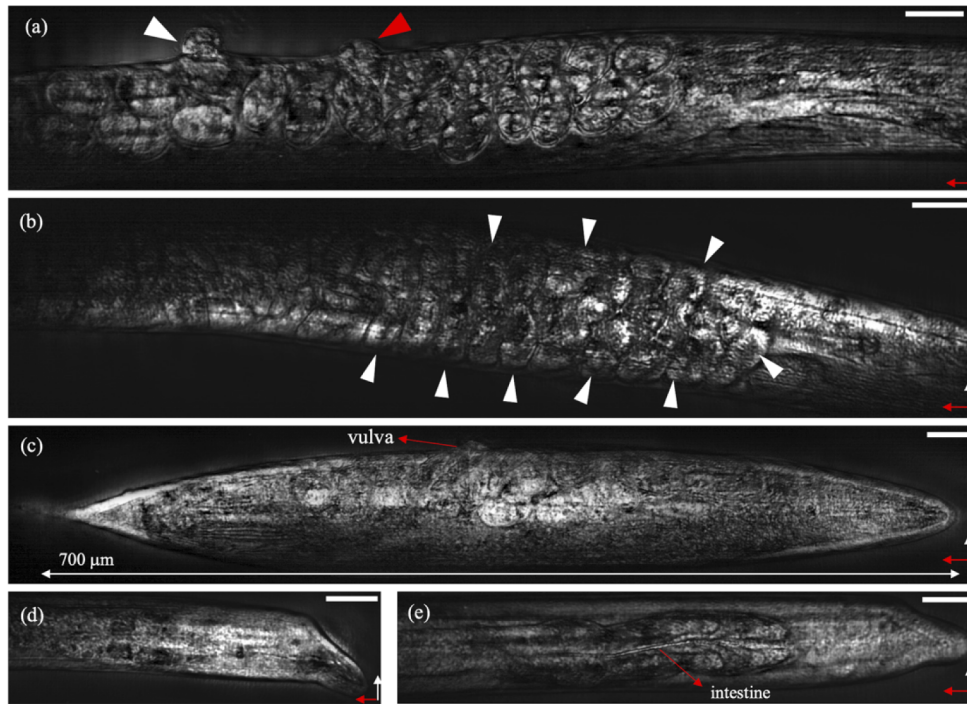


Fig. 5. (a) The protrusion caused by the *let-60* gene is visible (white arrowhead), and the difference between vulva (red arrowhead) and psuedovulva (white arrowhead) can be distinguished. (b) A large number of eggs are visible in the middle body of the mutant worm. (c) Dumpy worm, the presence of vulva and eggs indicating worm is in the adult stage but shorter than an adult wild-type *C. elegans*. (d) and (e) head of the CB64 strain. Scale bar = 50 μm . White and red arrows showing galvo scanning and spectrally encoded direction respectively.

Accumulation of eggs inside the MT1082 adult *C. elegans* is clearly recognized when Fig. 5(b) is compared with Fig. 3(a) of WT adult *C. elegans*. SECM's ability in high-speed confocal imaging of *C. elegans* eggs can enable automated quantification of egg size and quantity, which is critical for studies focusing on *egl-1* regulation. In such studies, *C. elegans* *egl-1* regulation is often correlated with the restriction of the BH3-only proteins in mammals, which are activated by stress signals and are in the Bcl-2 family of proteins that control the mitochondrial pathway to apoptosis [41].

Reduction or loss of function in some cuticle collagen genes has resulted in a phenotype termed as dumpy (*dpy*), causing a significant decrease in worms' length, increased body diameter, and a delay in their growth and development [42]. For instance, the CB61 *C. elegans*, showing a loss of function in the *dpy-5* gene (allele *e-61*), are used to investigate their dumpy phenotypes of smaller size and slow motion [42]. The *dpy-5* gene that makes the worms dumpy can cause diseases in humans such as osteogenesis imperfecta [43]. Figure 5(c) is a representative image of a dumpy CB61 adult worm. This worm has a vulva and eggs, both of which are indicators of the adult stage; nevertheless, the length of the worm is $\sim 700\ \mu\text{m}$ which is significantly shorter than that of WT *C. elegans* in the adult stage.

The gene *e648* can cause defects in the head epidermal morphogenesis of *C. elegans* and eventually lead to the formation of a notched head [44]. That is, instead of an oval shape head, the CB648 strain exhibits irregularities on top of the head which can clearly be seen in the

SECM image of Fig. 5(d). The CB648 life cycle is longer than WT *C. elegans*, which takes them longer to reach the adult stage. SECM's ability to resolve the irregularities caused by e648 gene mutation is key for human disease models focusing on eye developmental defects such as aniridia and peters anomaly [44]. Figure 5 images of mutant *C. elegans* demonstrate feasibility of resolving several key mutation-induced structural hallmarks with SECM.

4. Limitations and future work

As a variant of reflectance confocal microscopy, the source of contrast in SECM is the scattering/reflection of light. To that end, SECM images provide information only on geometry and internal tissue structures of *C. elegans* and do not offer any insight into chemistry or molecular make up of tissue. Chemical specificity can potentially be achieved in SECM by administration of antibody-conjugated contrast agents targeting the molecule(s) of interest. The SECM system used in this study incorporated a light source with center wavelength of 1.3 μm . While smaller center wavelengths (e.g., 800 nm) offer better imaging resolution, we believe that the 1.3 μm center wavelength is a better fit for SECM imaging in microfluidic platforms because these devices are normally based on poly-dimethylsiloxane (PDMS) which exhibits its visible-NIR minimal light absorption at 1320 nm [45]. Reliable and repeatable positioning of *C. elegans* in the field of view of the SECM system is another potential challenge of high-throughput imaging. To overcome this issue, we are currently developing microfluidic platforms for automated loading and unloading of the worms in the system. Once this improvement is achieved, we intend to examine the possibility of performing high-throughput imaging of worm populations in microfluidic platforms (as shown in spectrally encoded flow cytometry [46]). Figure 6 depicts the conceptual design of such system where worm cross sections are continuously imaged as population of worms are passed through the microchannel. Post-processing of acquired images can potentially enable 3D reconstruction of worm geometry and structures. Given the 147 KHz line rate of developed system the 60 μm -diameter of the microchannel can be imaged with a 0.4 μm spatial sampling period at a temporal rate of 980 frames per second. Such high imaging speed can theoretically accommodate 3D confocal imaging of *C. elegans* at an unprecedented speed of ~ 10 worms per second with voxel size of $0.4 \times 0.4 \times 10 \mu\text{m}^3$.

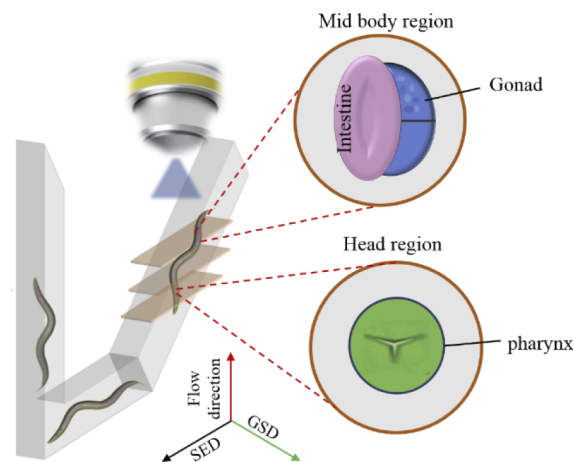


Fig. 6. Conceptual design of SECM system for high-throughput 3D imaging of *C. elegans*. GSD: Galvo scanning direction, SED: Spectrally encoded direction.

5. Conclusions

A near infrared SECM system with an imaging line rate of up to 147 KHz has been developed to examine the feasibility of label-free high-speed confocal imaging of *C. elegans*. Performance tests indicate the system has a lateral and axial resolution of $\sim 2\ \mu\text{m}$ and $10\ \mu\text{m}$. SECM images of WT and mutant *C. elegans* are presented and discussed. These results suggest that the developed system offers the resolution and contrast needed for visualization of key internal organs such as the pharyngeal region (mouth, isthmus, posterior bulb, and terminal bulb), vulva, egg, hatched larvae and lumen of the intestine. Mutation-induced structural hallmarks of MT2124, MT1082, CB61, and CB648 strains were also clearly resolved. This feasibility study demonstrates the promise of SECM for high-speed confocal imaging of *C. elegans* and is expected to open the door for downstream integration of SECM into microfluidic platforms to enable high-throughput physiological and behavioral phenotype screening of *C. elegans* populations.

Funding. Ontario Ministry of Colleges and Universities (Early Researcher Award 2019-0086); Natural Sciences and Engineering Research Council of Canada (RGPIN-2015-03666, RGPIN-2020-06140).

Acknowledgments. N.T. is grateful to the Natural Sciences and Engineering Research Council of Canada for the award of Discovery grant. PR is grateful to the Natural Sciences and Engineering Research Council of Canada for the award of Discovery grant and to the Government of Ontario for the Early Researcher Award.

Disclosures. The authors declare that there are no conflicts of interest related to this article.

Data availability. Data underlying the results presented in this paper are not publicly available at this time but may be obtained from the authors upon reasonable request.

References

1. K. Youssef, A. Tandon, and P. Rezai, "Studying Parkinson's disease using *Caenorhabditis elegans* models in microfluidic devices," *Integr. Biol.* **11**(5), 186–207 (2019).
2. M. Markaki and N. Tavernarakis, "Modeling human diseases in *Caenorhabditis elegans*," *Biotechnol. J.* **5**(12), 1261–1276 (2010).
3. M. J. Rodríguez-Palero, A. López-Díaz, R. Marsac, J.-E. Gomes, M. Olmedo, and M. Artal-Sanz, "An automated method for the analysis of food intake behaviour in *Caenorhabditis elegans*," *Sci. Rep.* **8**(1), 3633 (2018).
4. J. F. Cooper and J. M. Van Raamsdonk, "Modeling Parkinson's disease in *C. elegans*," *J. Parkinson's Dis.* **8**(1), 17–32 (2018).
5. A. Schlotterer, G. Kukudov, F. Bozorgmehr, H. Hutter, X. Du, D. Oikonomou, Y. Ibrahim, F. Pfisterer, N. Rabbani, and P. Thornalley, "C. elegans as model for the study of high glucose-mediated life span reduction," *Diabetes* **58**(11), 2450–2456 (2009).
6. J. F. Cooper, D. J. Dues, K. K. Spielbauer, E. Machiela, M. M. Senchuk, and J. M. Van Raamsdonk, "Delaying aging is neuroprotective in Parkinson's disease: a genetic analysis in *C. elegans* models," *npj Parkinson's Dis.* **1**(1), 15022–12 (2015).
7. P. M. Medina, J. M. Ponce, and C. A. Cruz, "Revealing the anticancer potential of candidate drugs in vivo using *Caenorhabditis elegans* mutant strains," *Translational Oncology* **14**(1), 100940 (2021).
8. A. S. Maddox and P. S. Maddox, "High-resolution imaging of cellular processes in *Caenorhabditis elegans*," *Methods Cell Biol.* **107**, 1–34 (2012).
9. C. Martin, T. Li, E. Hegarty, P. Zhao, S. Mondal, and A. Ben-Yakar, "Line excitation array detection fluorescence microscopy at 0.8 million frames per second," *Nat. Commun.* **9**(1), 1–10 (2018).
10. J. Van Krugten, K. K. Taris, and E. J. G. Peterman, "Imaging adult *C. elegans* live using light-sheet microscopy," *J. Microsc.* **281**(3), 214–223 (2021).
11. G. Filippidis, C. Kouloumentas, G. Voglis, F. Zacharopoulou, T. G. Papazoglou, and N. Tavernarakis, "Imaging of *Caenorhabditis elegans* neurons by second-harmonic generation and two-photon excitation fluorescence," *J. Biomed. Opt.* **10**(2), 024015 (2005).
12. S. Coquoz, P. J. Marchand, A. Bouwens, L. Mouchiroud, V. Sorrentino, D. Szlag, J. Auwerx, and T. Lasser, "Label-free three-dimensional imaging of *Caenorhabditis elegans* with visible optical coherence microscopy," *PLoS One* **12**(7), e0181676 (2017).
13. G. J. Tearney, R. H. Webb, and B. E. Bouma, "Spectrally encoded confocal microscopy," *Opt. Lett.* **23**(15), 1152–1154 (1998).
14. C. Boudoux, "Wavelength swept spectrally encoded confocal microscopy for biological and clinical applications," Massachusetts Institute of Technology, 2007).
15. H. Yoo, D. Kang, A. J. Katz, G. Y. Lauwers, N. S. Nishioka, Y. Yagi, P. Tanpowpong, J. Namati, B. E. Bouma, and G. J. Tearney, "Reflectance confocal microscopy for the diagnosis of eosinophilic esophagitis: a pilot study conducted on biopsy specimens," *Gastrointestinal Endoscopy* **74**(5), 992–1000 (2011).

16. D. Kang, S. C. Schlachter, R. W. Carruth, M. Kim, T. Wu, N. Tabatabaei, A. R. Soomro, C. N. Grant, M. Rosenberg, and N. S. Nishioka, "Large-area spectrally encoded confocal endomicroscopy of the human esophagus in vivo," *Lasers Surg. Med.* **49**(3), 233–239 (2017).
17. N. Tabatabaei, D. Kang, M. Kim, T. Wu, C. N. Grant, M. Rosenberg, N. S. Nishioka, P. E. Hesterberg, J. Garber, and Q. Yuan, "Clinical translation of tethered confocal microscopy capsule for unsedated diagnosis of eosinophilic esophagitis," *Sci. Rep.* **8**(1), 2631 (2018).
18. J. Kim, D. Kang, and D. Gweon, "Spectrally encoded slit confocal microscopy," *Opt. Lett.* **31**(11), 1687–1689 (2006).
19. S. Kim, J. Hwang, J. Heo, S.-H. Ryu, D. Lee, S.-H. Kim, S. J. Oh, and C. Joo, "Spectrally encoded slit confocal microscopy using a wavelength-swept laser," *J. Biomed. Opt.* **20**(3), 036016 (2015).
20. E. E. Freeman, A. Semeere, H. Osman, G. Peterson, M. Rajadhyaksha, S. González, J. N. Martin, R. R. Anderson, G. J. Tearney, and D. Kang, "Smartphone confocal microscopy for imaging cellular structures in human skin in vivo," *Biomed. Opt. Express* **9**(4), 1906–1915 (2018).
21. C. Gong, D. B. Stratton, C. N. Curiel-Lewandrowski, and D. Kang, "Speckle-free, near-infrared portable confocal microscope," *Appl. Opt.* **59**(22), G41–G46 (2020).
22. D. Yelin, B. E. Bouma, S. H. Yun, and G. J. Tearney, "Double-clad fiber for endoscopy," *Opt. Lett.* **29**(20), 2408–2410 (2004).
23. C. Boudoux, S. H. Yun, W.-Y. Oh, W. M. White, N. V. Iftimia, M. Shishkov, B. E. Bouma, and G. J. Tearney, "Rapid wavelength-swept spectrally encoded confocal microscopy," *Opt. Express* **13**(20), 8214–8221 (2005).
24. J. Hwang, S. Kim, J. Heo, D. Lee, S. Ryu, and C. Joo, "Frequency-and spectrally-encoded confocal microscopy," *Opt. Express* **23**(5), 5809–5821 (2015).
25. S. C. Schlachter, D. Kang, M. J. Gora, P. Vacas-Jacques, T. Wu, R. W. Carruth, E. J. Wilsterman, B. E. Bouma, K. Woods, and G. J. Tearney, "Spectrally encoded confocal microscopy of esophageal tissues at 100 kHz line rate," *Biomed. Opt. Express* **4**(9), 1636–1645 (2013).
26. A. Agrawal, T. J. Pfefer, P. D. Woolliams, P. H. Tomlins, and G. Nehmetallah, "Methods to assess sensitivity of optical coherence tomography systems," *Biomed. Opt. Express* **8**(2), 902–917 (2017).
27. T. Stiernagle, "Maintenance of *C. elegans*," in *Wormbook* (Wormbook, 2006).
28. M. Porta-de-la-Riva, L. Fontrodona, A. Villanueva, and J. Cerón, "Basic *Caenorhabditis elegans* methods: synchronization and observation," *Journal of visualized experiments: JoVE* (2012).
29. S. Shaham, "Wormbook: methods in cell biology," in *Wormbook* (Wormbook, 2006).
30. W. R. Schafer, "Genetics of egg-laying in worms," *Annu. Rev. Genet.* **40**(1), 487–509 (2006).
31. L. McMahon, J. M. Muriel, B. Roberts, M. Quinn, and I. L. Johnstone, "Two sets of interacting collagens form functionally distinct substructures within a *Caenorhabditis elegans* extracellular matrix," *Mol. Biol. Cell* **14**(4), 1366–1378 (2003).
32. A. D. Chisholm and H. R. Horvitz, "Patterning of the *Caenorhabditis elegans* head region by the Pax-6 family member *vab-3*," *Nature* **377**(6544), 52–55 (1995).
33. A. J. Nichols and C. L. Evans, "Video-rate scanning confocal microscopy and microendoscopy," *JoVE* **56**(56), e3252 (2011).
34. O. Haeberlé, M. Ammar, H. Furukawa, K. Tenjimayashi, and P. Török, "Point spread function of optical microscopes imaging through stratified media," *Opt. Express* **11**(22), 2964–2969 (2003).
35. S. Preibisch, S. Saalfeld, and P. Tomancak, "Globally optimal stitching of tiled 3D microscopic image acquisitions," *Bioinformatics* **25**(11), 1463–1465 (2009).
36. S. Hashmi, Y. Wang, R. S. Parhar, K. S. Collison, W. Conca, F. Al-Mohanna, and R. Gaugler, "A *C. elegans* model to study human metabolic regulation," *Nutr. Metab.* **10**(1), 31 (2013).
37. K. T. Jones and K. Ashrafi, "Caenorhabditis elegans as an emerging model for studying the basic biology of obesity," *Dis. Models Mech.* **2**(5-6), 224–229 (2009).
38. F. Chen, A. D. MacKerell, Y. Luo, and P. Shapiro, "Using *Caenorhabditis elegans* as a model organism for evaluating extracellular signal-regulated kinase docking domain inhibitors," *J. Cell Commun. Signal.* **2**(3-4), 81–92 (2008).
39. D. J. Reiner, V. González-Pérez, C. J. Der, and A. D. Cox, "Use of *Caenorhabditis elegans* to evaluate inhibitors of Ras function in vivo," *Methods Enzymol.* **439**, 425–449 (2008).
40. B. Conradt and H. R. Horvitz, "The *C. elegans* protein EGL-1 is required for programmed cell death and interacts with the Bcl-2-like protein CED-9," *Cell* **93**(4), 519–529 (1998).
41. R. Nehme and B. Conradt, "egl-1: a key activator of apoptotic cell death in *C. elegans*," *Oncogene* **27**(S1), S30–S40 (2008).
42. C. Thacker, J. A. Sheps, and A. M. Rose, "Caenorhabditis elegans dpy-5 is a cuticle procollagen processed by a proprotein convertase," *Cell. Mol. Life Sci.* **63**(10), 1193–1204 (2006).
43. M. Watanabe, N. Mitani, N. Ishii, and K. Miki, "A mutation in a cuticle collagen causes hypersensitivity to the endocrine disrupting chemical, bisphenol A, in *Caenorhabditis elegans*," *Mutat. Res., Fundam. Mol. Mech. Mutagen.* **570**(1), 71–80 (2005).
44. H. N. Cinar and A. D. Chisholm, "Genetic analysis of the *Caenorhabditis elegans* pax-6 locus: roles of paired domain-containing and nonpaired domain-containing isoforms," *Genetics* **168**(3), 1307–1322 (2004).
45. C. Markos, K. Vlachos, and G. Kakarantzas, "Guiding and thermal properties of a hybrid polymer-infused photonic crystal fiber," *Opt. Mater. Express* **2**(7), 929–941 (2012).
46. A. Zeidan, L. Golan, and D. Yelin, "In vitro hematocrit measurement using spectrally encoded flow cytometry," *Biomed. Opt. Express* **7**(10), 4327–4334 (2016).